Southern Hemisphere Winter Storm Tracks Respond Differently to Low and High CO_2 Forcings

IVAN MITEVSKI,[a] REI CHEMKE,[b] CLARA ORBE,[a,c] AND LORENZO M. POLVANI[a,d]

[a] *Department of Applied Physics and Applied Mathematics, Columbia University, New York, New York*
[b] *Department of Earth and Planetary Sciences, Weizmann Institute of Science, Rehovot, Israel*
[c] *NASA Goddard Institute for Space Studies, New York, New York*
[d] *Lamont-Doherty Earth Observatory, Columbia University, Palisades, New York*

(Manuscript received 21 December 2023, in final form 22 June 2024, accepted 14 July 2024)

ABSTRACT: In the Southern Hemisphere, Earth system models project an intensification of winter storm tracks by the end of the twenty-first century. Previous studies using idealized models showed that storm track intensity saturates with increasing temperatures, suggesting that the intensification of the winter storm tracks might not continue further with increasing greenhouse gases. Here, we examine the response of midlatitude winter storm tracks in the Southern Hemisphere to increasing CO_2 from two to eight times preindustrial concentrations in more realistic Earth system models. We find that at high CO_2 levels (beyond $4\times CO_2$), winter storm tracks no longer exhibit an intensification across the extratropics. Instead, they shift poleward, weakening the storm tracks at lower midlatitudes and strengthening at higher midlatitudes. By analyzing the eddy kinetic energy (EKE) budget, the nonlinear storm-track response to an increase in CO_2 levels in the lower midlatitudes is found to stem from a scale-dependent conversion of eddy available potential energy to EKE. Specifically, in the lower midlatitudes, this energy conversion acts to oppositely change the EKE of long and short scales at low CO_2 levels, but at high CO_2 levels, it mostly reduces the EKE of shorter scales, resulting in a poleward shift of the storms. Furthermore, we identify a "tug of war" between the upper and lower temperature changes as the primary driver of the nonlinear-scale-dependent EKE response in the lower midlatitudes. Our results suggest that in the highest emission scenarios beyond the twenty-first century, the storm tracks' response may differ in magnitude and latitudinal distribution from projected changes by 2100.

SIGNIFICANCE STATEMENT: The Southern Hemisphere winter storm track is projected to intensify by the end of the century, with the most significant intensification occurring in the higher midlatitudes. However, we show that the intensification is not a linear function of the radiative forcing associated with increasing CO_2 levels. In fact, our study shows a poleward shift at very high CO_2 levels, with the storm track moving southward. This suggests that the Southern Hemisphere winter storm track may require time-sensitive adaptation strategies, as the impacts of global warming on the storm track may not be a linear function of CO_2 concentration in the atmosphere.

KEYWORDS: Atmospheric circulation; Baroclinic flows; Dynamics; Eddies

1. Introduction

Extratropical storm tracks transport heat, momentum, and moisture, thereby directly influencing Earth's hydrological cycle (Harvey et al. 2014; Schwierz et al. 2010). These storm tracks play a significant role in shaping regional weather and climate by impacting the variability of precipitation, temperature, and winds in extratropical regions (Pfahl and Wernli 2012; Yau and Chang 2020; Chang et al. 2022). Any future changes in storm tracks resulting from increased greenhouse gas (GHG) emissions will have consequential effects on regional climate. Therefore, understanding how storm tracks will change in a warmer world becomes a critically important question to address.

The extratropical storm tracks consist of transient eddies that extract their energy from the mean available potential energy (MAPE) via the process of baroclinic instability (Lorenz 1955; O'Gorman 2010). Since MAPE depends on both the horizontal (meridional) and vertical (static stability) temperature gradients (Lorenz 1955; Peixóto and Oort 1974), changes in the temperature gradients in a warmer climate will directly impact the storm tracks. For example, in a warmer climate, the upper tropical troposphere is projected to warm more than the upper polar troposphere, leading to a stronger upper meridional temperature gradient and increased static stability at lower midlatitudes. Conversely, near the surface, the polar regions are expected to warm more than the tropics, decreasing the lower meridional temperature gradient and static stability at higher midlatitudes (Butler et al. 2010). These opposing effects are expected to differently affect the response of the storms to anthropogenic emissions.

Numerous Earth system model studies have extensively explored the future response of storm tracks to increased GHG concentrations (Yin 2005; Chang et al. 2012; Zappa et al. 2013; Harvey et al. 2014; Lehmann et al. 2014; Harvey et al. 2020; Priestley and Catto 2022). In the Northern Hemisphere, these studies suggest a weakening of summer (JJA) storm tracks, while winter (DJF) storm tracks are expected to strengthen by the end of the twenty-first century only over the

Corresponding author: Ivan Mitevski, im2527@columbia.edu

DOI: 10.1175/JCLI-D-23-0758.1

North Atlantic/western Europe. In the Southern Hemisphere, summer (DJF) storm tracks are projected to shift poleward, while winter (JJA) storm tracks are anticipated to intensify. It should be noted that these changes are seen in models using Eulerian metrics for the storm tracks (e.g., eddy kinetic energy), while Lagrangian-based metrics might yield different results (Priestley and Catto 2022; Zappa et al. 2013). Some of these storm-track responses have already been observed in recent decades, including a shift in Southern Hemisphere (SH) summer (Fyfe 2003; Bender et al. 2012) largely driven by stratospheric ozone depletion (Polvani et al. 2011), an intensification in SH winter (Chemke et al. 2022a), and a weakening in NH summer (Coumou et al. 2015; Chang et al. 2016). It is important to acknowledge that most previous work has primarily focused on the future storm-track response under scenarios involving CO_2-quadrupling by the end of this century [e.g., representative concentration pathway 8.5 (RCP8.5) and shared socioeconomic pathway 5-8.5 (SSP5-8.5)]. Nevertheless, without any mitigation policy, the CO_2 concentrations are expected to continue to increase beyond 2100. For example, the highest emission SSP5-8.5 projects a transient increase in greenhouse gas forcing up to $8\times CO_2$, relative to preindustrial (PI) values, by the year 2250 (Meinshausen et al. 2020). Therefore, a more comprehensive understanding of the storm-track response at CO_2 levels above $4\times CO_2$ is essential.

Furthermore, previous idealized studies (e.g., O'Gorman and Schneider 2008) have revealed a possible nonlinear behavior of storm tracks in response to global warming. Specifically, these studies demonstrated that the eddy kinetic energy (EKE) exhibits a maximum at current surface temperatures and decreases under both warmer and colder surface temperature conditions. Considering that other studies have indicated the potential for nonlinear variations in EKE in a warmer world beyond the twenty-first century (Orbe et al. 2023), and given our expectation of reaching high CO_2 levels in the future, we here systematically investigate the response of storm tracks at CO_2 forcing levels above $4\times CO_2$ using more realistic Earth system model simulations. This endeavor is important because understanding and predicting how storm tracks will respond in future warming scenarios beyond the twenty-first century is essential for developing effective adaptation and mitigation strategies in the next century, particularly in the event of a nonlinear response.

Our primary objective here is to address the question regarding the linearity of the intensification of the winter storm tracks in the Southern Hemisphere in relation to increasing CO_2 concentrations. We focus on the storm tracks in the Southern Hemisphere, as they exhibit a nearly zonally symmetric structure (Chemke et al. 2022a), which not only allows us to revisit the nonlinear behavior of the storms' intensity, previously found in zonally symmetric idealized models (O'Gorman and Schneider 2008), but also because such zonal symmetry is necessary for conducting a zonal spectral analysis. As we will show below, the storms' spectral response to different CO_2 levels is a key component in their nonlinear behavior.

2. Methods

a. Models

We utilize two Earth system models: the large ensemble version of the Community Earth System Model-Large Ensemble (CESM-LE) and the NASA Goddard Institute for Space Studies Model E2.1-G (GISS-E2.1-G). The CESM-LE model incorporates the Community Atmosphere Model, version 5 (CAM5), with 30 vertical levels (with the model top of 3.6 hPa), along with the Parallel Ocean Program version 2 (POP2) featuring 60 vertical levels. It employs a 1° horizontal resolution across all model components (Kay et al. 2015). The GISS-E2.1-G model includes a 40-level atmosphere (model top of 0.1 hPa) with a $2^\circ \times 2.5^\circ$ latitude/longitude resolution and a 40-level GISS Ocean v1 (GO1) component with a 1° horizontal resolution (Kelley et al. 2020). This specific GISS model configuration contributed output to the phase 6 of Coupled Model Intercomparison (CMIP6) and is referred to as "GISS-E2-1-G."

In addition, we analyze model experiment output from the extended RCP8.5 scenario from CMIP5, and the SSP5-8.5 from CMIP6. These scenarios run up to year 2300 with up to $7.6\times CO_2$ relative to PI levels. We use seven models in total because those were the only models for which we could find output for daily variables for the zonal and meridional winds. The CMIP5 models used are MPI-ESM-LR, IPSL-CM5A-LR, and CSIRO-Mk3-6-0, and the CMIP6 models are CanESM5, ACCESS-ESM1-5, MRI-ESM2-0, and EC-Earth3-Veg.

b. Experiments

In our study, we conduct abrupt-CO_2 experiments using both CESM-LE and GISS-E2.1-G models, applying forcings of $2\times$, $3\times$, $4\times$, $5\times$, $6\times$, $7\times$, and $8\times CO_2$, relative to preindustrial values. In these experiments, trace gases, ozone concentrations, aerosols, and other forcings are maintained at PI values. The integration period for all runs is set to 150 years, starting from PI conditions, following a similar protocol to the CMIP6 guidelines for $4\times CO_2$ runs. The response to abrupt-CO_2 forcing is assessed by comparing the last 50 years of each experiment with the corresponding PI control run.

To verify that our results also hold under a more realistic increase in CO_2, we conduct transient-CO_2 experiments using both models. These experiments begin from PI conditions, similar to the abrupt-CO_2 experiments. The CO_2 concentration is then increased at a rate of 1% per year (1pctCO_2) for a duration of 215 years, reaching slightly above $8\times CO_2$. The response to transient CO_2 forcing is assessed by comparing this experiment (10-yr average over the $n\times CO_2$ value) with a PI control run. The response for the RCP8.5 and SSP5-8.5 scenario runs is calculated by contrasting the average of the last 20 years of each century (e.g., years 2080–2100 for the twenty-first century) to the PI control run.

c. EKE

Following previous studies (O'Gorman and Schneider 2008; Chang et al. 2012; Coumou et al. 2015; Chemke and Ming 2020; Chemke et al. 2022b), we assess the intensity of

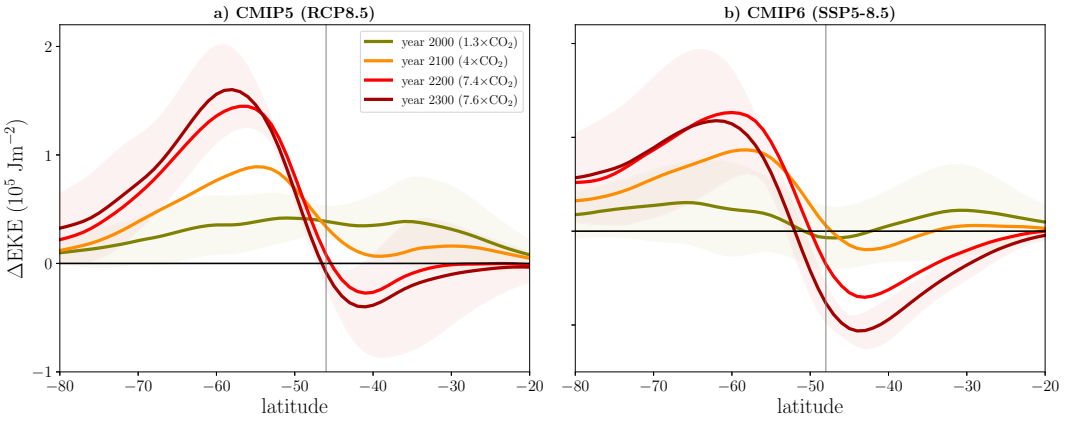

FIG. 1. Winter zonal EKE response (relative to PI control run) in the SH from CMIP models with extended RCP8.5 and SSP5-8.5 scenarios (see section 2). The solid lines show the CMIP mean, and the shading (only for years 2000 and 2300) shows one standard deviation across the models. The latitude of the maximum EKE for the PI control run is shown in gray vertical lines.

the winter (June–August) storm tracks in the Southern Hemisphere using the vertically integrated transient EKE,

$$\mathrm{EKE} = \frac{1}{2g}\int_0^{p_s}(u'^2 + v'^2)dp, \tag{1}$$

where g is the gravitational constant, p_s is the surface pressure, u and v are the zonal and meridional wind, respectively, and prime denotes the deviation from the monthly mean. We define the eddy components, u' and v', as deviations from the monthly mean since daily wind output in our CESM-LE experiments is available on only a few vertical levels. Nevertheless, defining the eddies using a bandpass filter of 2–6 days does not change our results.

Additionally, the EKE spectrum is computed using a one-dimensional Fourier analysis in the zonal direction at each latitude (Saltsman 1957), following the methodology employed in Chemke and Ming (2020),

$$\mathrm{EKE}_k = \frac{1}{2g}\int_0^{p_s}(|u'_k|^2 + |v'_k|^2)dp, \tag{2}$$

where subscript k denotes the zonal wavenumber and the absolute value signs indicate the modulus (as the spectral amplitudes are complex numbers).

d. Spectral EKE budget

To identify the factors responsible for the changes in the EKE spectrum, we follow previous studies (Chemke and Kaspi 2015; Chemke and Ming 2020; Saltsman 1957) and calculate the EKE_k budget,

$$\frac{\partial \mathrm{EKE}_k}{\partial t} = \mathrm{PK}_k + \mathrm{EM}_k + \mathrm{EE}_k + \mathrm{F}_k. \tag{3}$$

The term PK_k corresponds to the conversion of eddy available potential energy to eddy kinetic energy,

$$\mathrm{PK}_k = -\frac{2}{g}\int_0^{p_s}\mathrm{Re}(\mathbf{u}'^*_k \cdot \nabla\varphi'_k)dp, \tag{4}$$

where $\mathbf{u}$ represents the horizontal velocity vector and φ is the geopotential. The asterisk symbol denotes the complex conjugate.

The term EM_k describes the transfer of kinetic energy between the eddies and the zonal mean flow, with the overbar indicating the zonal average and θ the latitude.

$$\mathrm{EM}_k = -\frac{2}{g}\int_0^{p_s}\mathrm{Re}\left\{u'^*_k \cdot \left[\overline{\mathbf{u}}\cdot\nabla u' + \mathbf{u}'\cdot\nabla\overline{u} - \frac{\overline{u}v'\tan(\theta)}{a} - \frac{u'\overline{v}\tan(\theta)}{a}\right]_k + v'^*_k \cdot \left[\overline{\mathbf{u}}\cdot\nabla v' + \mathbf{u}'\cdot\nabla\overline{v} + 2\frac{\overline{u}u'\tan(\theta)}{a}\right]_k\right\}dp. \tag{5}$$

The term EE_k represents the energy transfer between different waves (eddies of different wavenumbers). Finally, the term F_k incorporates the dissipation processes and is estimated as the residual in our budget calculation,

$$\mathrm{EE}_k = -\frac{2}{g}\int_0^{p_s}\mathrm{Re}\left[u'^*_k\left(\mathbf{u}'\cdot\nabla u' - \frac{u'v'\tan\theta}{a}\right)_k + v'^*_k\left(\mathbf{u}'\cdot\nabla v' + \frac{u'u'\tan\theta}{a}\right)_k\right]dp. \tag{6}$$

3. Results

a. The nonlinear behavior of the Southern Hemisphere EKE

We start by analyzing Southern Hemisphere wintertime EKE changes in the historical and the extended highest emission scenarios RCP8.5 (CMIP5) and SSP5-8.5 (CMIP6) up to the year 2300. In the historical runs by the year 2000 (average over 1980–2000), we find a minor EKE intensification (CMIP5) and no response (CMIP6) in the lower midlatitudes, and EKE intensification in the higher midlatitudes is shown in olive lines in Fig. 1. We define the lower and higher midlatitudes by averaging over 30° of latitude, starting from the latitude of the maximum EKE at the PI (vertical gray lines), extending equatorward and

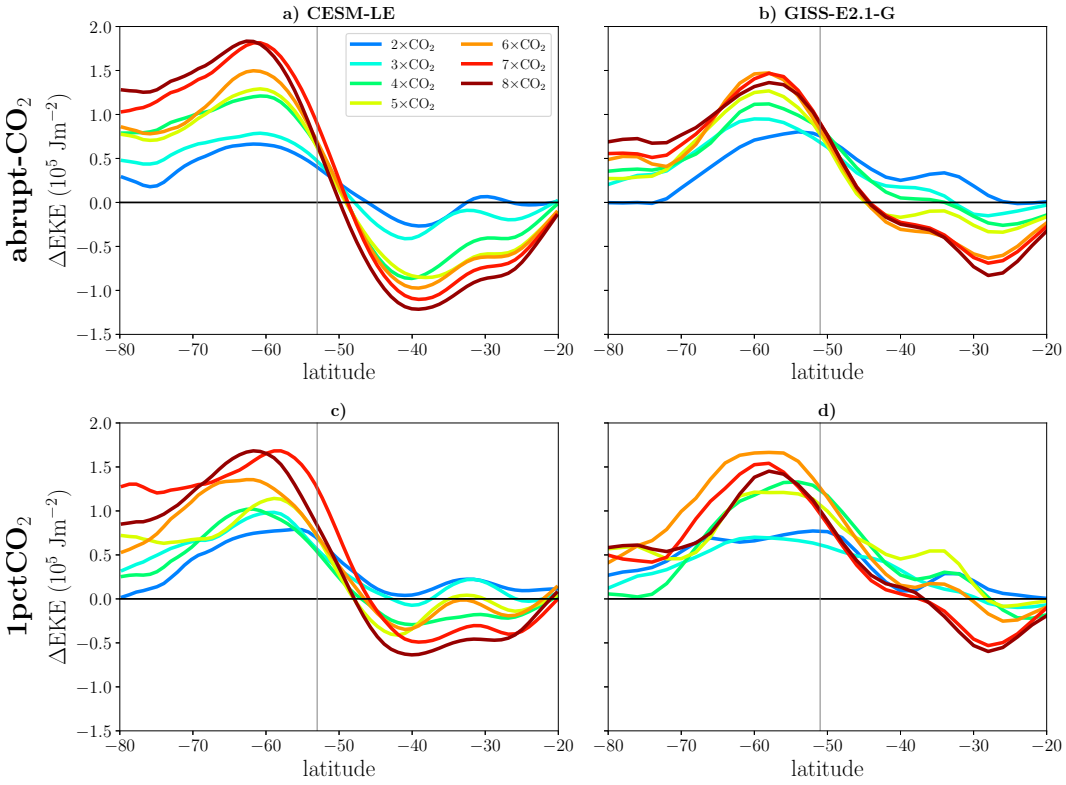

FIG. 2. SH winter (JJA) zonal mean EKE response to abrupt-CO_2 forcing in (a),(c) CESM-LE and (b),(d) GISS-E2.1-G models. (a),(b) The results from the abrupt-CO_2 runs and (c),(d) the findings from the transient 1pctCO_2 runs. The latitude of the maximum EKE for the PI control run is shown in gray vertical lines, and the latitudinal distribution is shown in Fig. A1.

poleward, respectively. By 2100, the highest emissions scenarios, which correspond to around 4×CO_2, result in EKE intensification at higher midlatitudes and almost no response in the lower midlatitudes (orange line). By the year 2200, these emission scenarios reach around 7.4×CO_2 (red line), and a stronger EKE intensification occurs at higher midlatitudes (poleward of the PI EKE maximum), and a larger EKE reduction occurs at the lower midlatitudes (equatorward of the PI EKE maximum), suggestive of a poleward shift of the storm tracks. From year 2200 to year 2300, the CO_2 values increase from 7.4× to 7.6×CO_2, which does not yield a further EKE intensification in the higher midlatitudes but a stronger reduction in the lower midlatitudes (dark red). In summary, we find a nonlinear EKE response in the lower midlatitudes in the extended high emission scenarios: EKE is at or above the PI value until 2100 and then weakens to year 2300.

To elucidate the nonlinear behavior of the EKE, we next analyze the wintertime EKE response in our abrupt-CO_2 forcing experiments up to 8×CO_2, which allows us to cleanly examine the evolution of the nonlinear EKE response. In the abrupt-CO_2 runs (Figs. 2a,b), we find that at low CO_2 levels (2× and 3×CO_2), the EKE intensifies more at higher midlatitudes than at lower midlatitudes (time series of both latitudinal bands shown in Fig. A2 in the appendix), consistent with the reported intensification by the end of this century in CMIP5 and CMIP6 models (Chang et al. 2012; Harvey et al. 2014). The EKE exhibits minor changes in the lower midlatitudes, with a slight reduction in the CESM-LE model (Fig. 2a) and some intensification in the GISS-E2.1-G model (Fig. 2b). As CO_2 levels increase (above 3×CO_2 for CESM-LE and 5×CO_2 for GISS-E2.1-G), extending up to 8×CO_2, the EKE continues to intensify in the higher midlatitudes (poleward of PI EKE maximum) while decreasing in the lower midlatitudes (equatorward of PI EKE maximum), resulting in a poleward shift of the EKE maximum (6° for CESM-LE and 4° for the GISS-E2.1-G model). This behavior is also evident under the more realistic transient 1pctCO_2 runs (Figs. 2c,d): even though the response is weaker for the lower midlatitude EKE weakening, the poleward shift is of a similar magnitude as in the abrupt-CO_2 runs (5° for CESM-LE and 4° for the GISS-E2.1-G model). To further illustrate the zonally symmetric shift of the Southern Hemisphere EKE toward higher midlatitudes, we present the EKE maps in Figs. A3 and A4, supporting our focus on studying the storm-track behavior from a zonal perspective.

Recently, Chemke and Ming (2020) demonstrated a scale-dependent response of projected EKE in twenty-first-century emission scenarios; while longer waves were found to intensify, shorter waves were found to weaken in the coming decades. It is thus crucial to examine the future changes in the storms as a function of their scale. To investigate this behavior

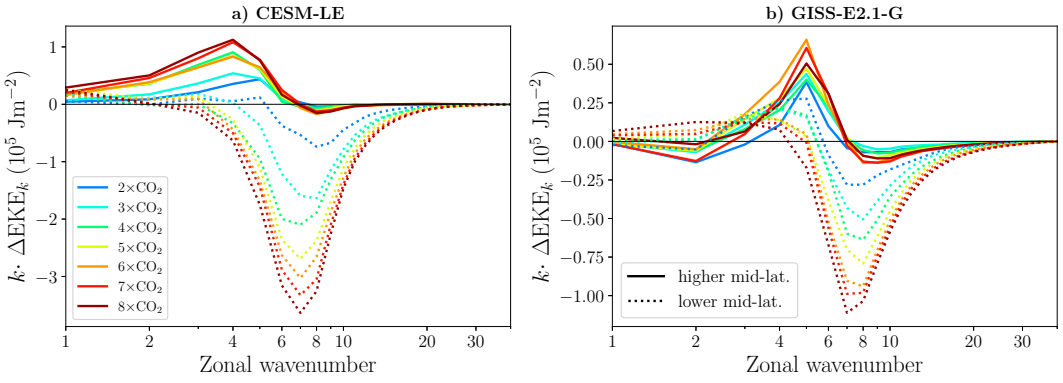

FIG. 3. The EKE_k response to abrupt-CO_2 forcing as a function of zonal wavenumber in (a) CESM-LE and (b) GISS-E2.1-G models. The solid lines represent an average over the higher midlatitudes (30° south of the latitude of zonally averaged EKE maximum from PI run), while the dotted lines indicate an average over the lower midlatitudes (30° north of the latitude of zonally averaged EKE maximum from PI run). The EKE response is multiplied by the zonal wavenumber to preserve the logarithmic x axis integral and is smoothed with a 3-point running means for plotting purposes. Values for 30° and 40°S are shown in Fig. A5 and PI values in Fig. A6.

in our experiments, we next examine the spectral structure of EKE [EKE_k, Eq. (2), Fig. 3]. At higher midlatitudes, EKE_k strengthens over wavenumbers 6 and below with increasing CO_2 concentrations, exhibiting a nearly monotonic increase, with a minor decrease at shorter scales. At lower midlatitudes, EKE_k weakens monotonically over shorter waves (wavenumbers 7 and above) with increasing CO_2, with a minor increase at longer scales (mainly not only in the GISS-E2.1-G but also to a lesser extent in the CESM-LE model at low CO_2 values). The scale-dependent changes at the lower midlatitudes might explain the delayed weakening of the EKE response over this region, i.e., pooling together the different EKE changes over different scales (as done in Fig. 2) will yield an overall minor EKE response for low CO_2 levels. Last, we note that while it is conceivable that a poleward shift of the EKE might yield a reduction in zonal wavenumber (Tamarin-Brodsky and Kaspi 2016, 2017; Tamarin and Kaspi 2017), the above scale-dependent changes are evident at each latitude (single latitudes shown in Fig. A5), and thus occur over different length scales, and are not a manifestation of a poleward shift of the storm tracks.

b. EKE_k Budget

We now investigate the underlying physical processes responsible for the scale-dependent response of EKE_k at the lower midlatitudes. We start by analyzing the budget equation of EKE_k (Chemke 2017; Chemke and Kaspi 2015; Saltsman 1957) as expressed in Eq. (3). The EKE_k budget shows four factors contributing to changes in EKE_k: the conversion from eddy available potential energy to EKE (PK_k), the transfer of energy between waves and the zonal mean flow (EM_k), the interactions between different waves (EE_k), and the dissipation processes (F_k).

The term that mostly contributes to the increase in EKE_k at higher midlatitudes and the decrease at lower midlatitudes is PK_k (Figs. 4a,b). All other terms have minor or mitigating effects. For example, in the lower midlatitudes, EM_k (Fig. 4c), EE_k (Figs. 4e,f), and F_k (Figs. 4g,h) act to increase EKE_k. In the higher midlatitudes, EE_k and F_k counteract the EKE_k increase. Furthermore, PK_k also captures the scale-dependent response of EKE_k in the lower midlatitudes (dotted lines in Figs. 4a,b). Such scale-dependent response at lower midlatitudes results in an overall minor PK_k, and thus EKE, changes at low CO_2 levels (once integrating over all wavenumbers). At high CO_2 levels, on the other hand, the reduction in PK_k at shorter scales overcomes the increase at longer scales, resulting in the overall weakening of EKE at lower midlatitudes. Thus, the nonlinear response of the EKE to CO_2 forcing (i.e., the intensification at lower and poleward shift at higher CO_2 concentrations) is due to the scale-dependent response of PK_k at lower midlatitudes. Additionally, we note that our PK_k equation includes a boundary term $[\nabla(\mathbf{u}_k'^{*}\varphi_k')]$ which we have not discussed. However, as one can see from Fig. A11b, that boundary term (which accounts for the energy transfer in and out of the latitudinal band) has a negligible impact on PK_k (Fig. A11a), so that the energy transfer across latitudinal bands does not contribute to the scale-dependent response. Last, the scale-dependent PK_k response in the lower midlatitudes may stem from the fact that in the preindustrial run, PK_k contributes to EKE_k reduction at longer scales and to EKE_k increase at shorter scales (Fig. A7).

The important role of PK_k for the EKE_k response suggests that baroclinic instability, which leads to the formation of transient midlatitude waves, likely plays a crucial role in the scale-dependent response of EKE_k. We thus next examine the changes in the Eady growth rate in these sets of simulations since it encapsulates the extraction of potential energy from the mean flow to the eddies and has been found by previous studies to adequately capture the EKE changes (Yin 2005; O'Gorman 2010; Lehmann et al. 2014; Wu et al. 2011). The Eady growth rate is defined as $\sigma \propto [(\partial\overline{T}/\partial y)/N]$, where $\partial\overline{T}/\partial y$ is the zonal-mean meridional temperature gradient and $N^2 = [(g/\theta)(\partial\overline{\theta}/\partial z)]$ is the static stability. First, we note that the Eady growth rate integrated over the troposphere (between

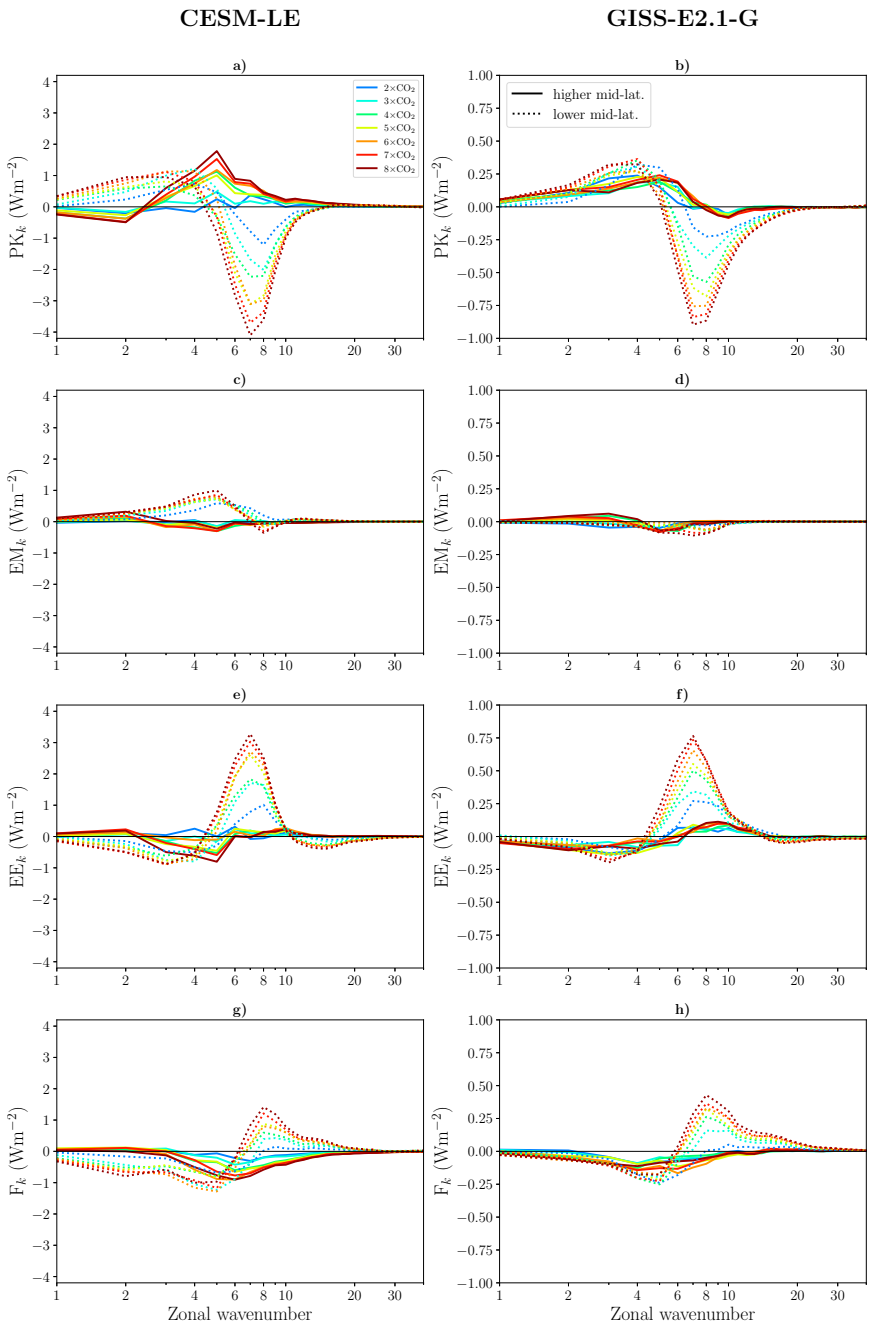

FIG. 4. Components of the EKE_k budget for the abrupt-CO_2 forcing experiments from Eq. (3): (a),(b) the conversion of eddy available potential energy to EKE (PK_k); (c),(d) the transfer of kinetic energy between the waves and the zonal mean flow (EM_k); (e),(f) the energy transfer between different waves (EE_k); and (g),(h) the dissipation processes (F_k). The solid lines represent higher midlatitudes, while the dotted lines indicate lower midlatitudes (defined in Fig. 3). The data from the (left) CESM-LE model and (right) GISS-E2.1-G model. The response is multiplied by the zonal wavenumber to ensure the preservation of the integral on the logarithmic x axis, and a 3-point running mean is applied for plotting purposes. PI values are shown in Fig. A7.

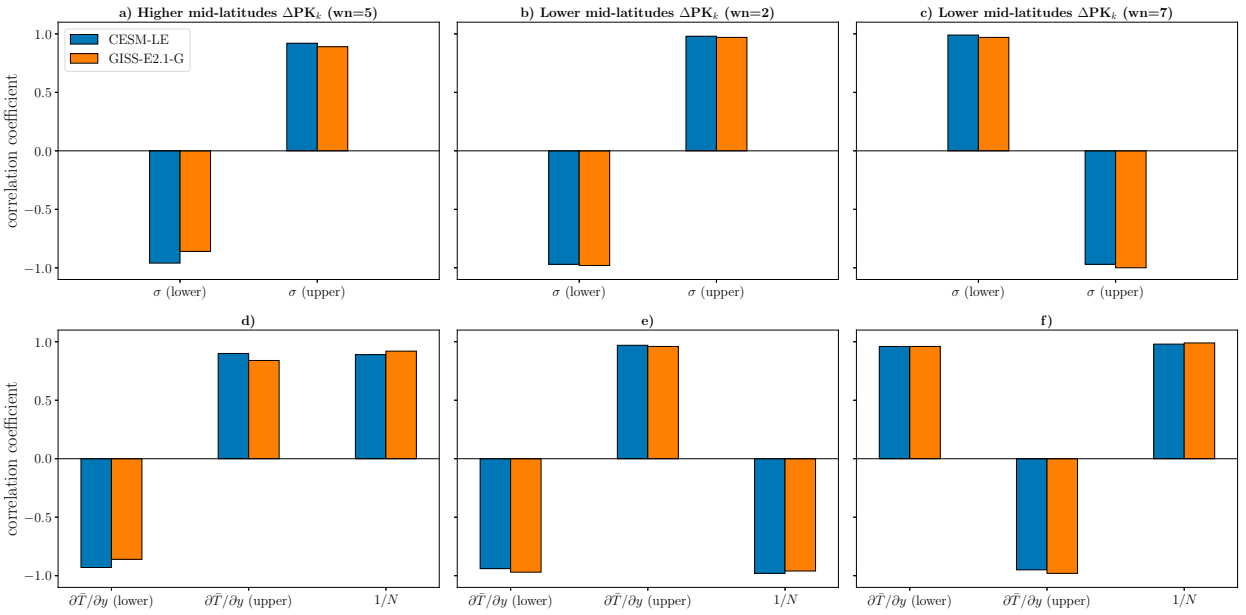

FIG. 5. (a)–(c) Correlation between PK$_k$ and lower and upper Eady growth rate from 2× to 8×CO$_2$ in the abrupt experiments. (d)–(f) Correlation between PK$_k$ and the components governing the Eady growth rate: the meridional temperature gradient $\partial\overline{T}/\partial y$ and the inverse of static stability 1/N. (a),(d) Higher midlatitudes and (b),(c),(e),(f) lower midlatitudes. (b),(e) The longer waves (wavenumber 2) at lower midlatitudes; and (c),(f) shorter waves (wavenumber 7).

250 hPa to the surface) is unable to fully capture the changes in EKE with CO$_2$ levels. For example, in CESM-LE, the vertically integrated Eady growth rate does not exhibit the same uniform changes as EKE (Fig. A8b). Similarly, the GISS-E2.1-G model (Fig. A8a) shows opposite behavior between the vertically integrated Eady growth rate and EKE at lower and higher midlatitudes. This suggests that the complex dynamics driving the scale-dependent response of EKE may not be adequately captured by the integrated vertical structure of the baroclinicity. Thus, given the opposite changes in upper- and lower-level baroclinicity (Harvey et al. 2014), we next examine the upper-level (integrated from 250 to 500 hPa) and lower-level (integrated from 500 hPa to the surface) Eady growth rate separately.

First, we find a high correlation ($r > 0.86$) between the PK$_k$ intensification at higher midlatitudes (estimated at zonal wavenumber 5, where the maximum PK$_k$ response occurs) and upper-level changes in the Eady growth rate across the CO$_2$ experiments (Fig. 5a; cf. Figs. A9 and A10 for the correlation plots). In contrast, the PK$_k$ intensification negatively correlates ($r < -0.85$) with lower Eady growth rate changes, i.e., the increase in PK$_k$ is correlated with a decrease in lower-level baroclinicity, and thus, physically, lower-level changes could not explain the PK$_k$ changes. These findings are consistent with previous studies that have established a link between the upper-level baroclinicity increase and EKE intensification at higher midlatitudes (Harvey et al. 2014; Yuval and Kaspi 2020).

Second, the PK$_k$ intensification at lower midlatitudes over longer scales also seems to be linked to upper-level changes in baroclinicity; the PK intensification (at wavenumber 2, where most of the intensification occurs) is highly correlated ($r > 0.97$) with upper-level changes in Eady growth rate across the CO$_2$ experiments, but negatively correlated ($r < -0.96$) with lower-level Eady growth rate changes (Fig. 5b). The reduction in PK$_k$ at lower midlatitudes over shorter scales is associated with lower-level changes in Eady growth rate, as the two fields are highly positively correlated ($r > 0.96$); the PK$_k$ reduction (at wavenumber 7, where most of the reduction occurs) is also negatively correlated with upper-level Eady growth rate changes (Fig. 5c). This suggests that the opposing behaviors in shorter and longer waves originate from the contrasting responses in low and high tropospheric Eady growth rates.

Further decomposition of the Eady growth rate into its different components reveals that the intensification at higher midlatitudes is linked to both the decrease in static stability (increase in 1/N) and increase in the upper-tropospheric meridional temperature gradient (Figs. 5d–f, correlation scatterplots in Fig. A10). Similar results were found for the projected PK$_k$ changes by the end of this century (Chemke and Ming 2020). In the lower midlatitudes, the PK$_k$ intensification for longer waves (wavenumber 2) is accompanied by the increase in the upper-tropospheric meridional temperature gradient (Fig. 5e), while the PK$_k$ decrease at shorter waves (wavenumber 7) is negatively correlated with the upper-level changes in meridional temperature gradient. This opposite behavior of large and small waves could stem from their different vertical extents. Specifically, Rivière (2011) showed that an increase in upper-level baroclinicity acts to increase the mean available potential energy. As a result, large waves, which have a large vertical extent, could extract more potential energy and become stronger. In contrast, short waves, which have

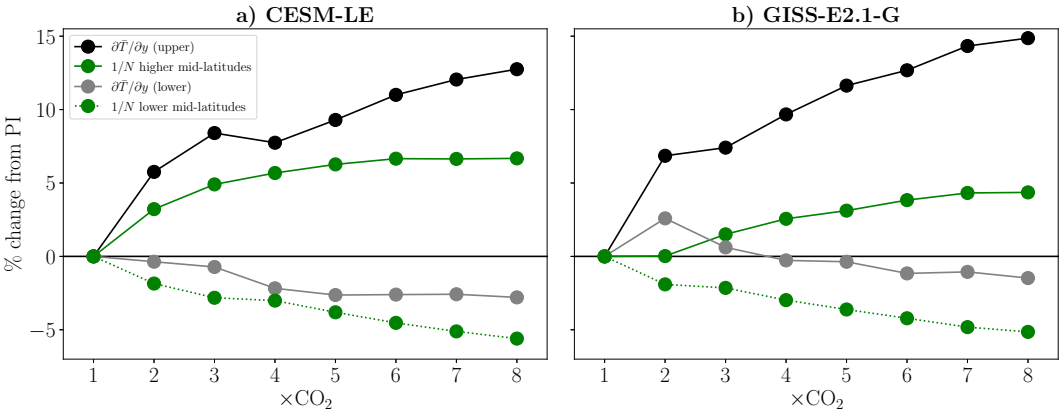

FIG. 6. Changes in the Eady growth components relative to PI values (%) for the abrupt-CO_2 forcing experiments: meridional temperature gradients ($\partial\overline{T}/\partial y$) in the upper (black) and lower (gray) troposphere and inverse of static stability ($1/N$) in the higher (full green) and lower midlatitudes (dotted green). (a) The CESM-LE and (b) the GISS-E2.1-G model.

small vertical extent, become more stable since an increase in upper-level baroclinicity also increases the vertical distance between levels of opposite meridional potential vorticity gradients.

In addition to the above effect, the PK_k decrease at shorter waves in the lower midlatitudes is associated with the increase in static stability and the weakening of the lower-tropospheric temperature gradient (Fig. 5f). The lower-tropospheric gradient is expected to weaken, and the static stability is expected to increase in the lower midlatitudes in a warmer world, reducing atmospheric baroclinicity and EKE (Lim and Simmonds 2009; Harvey et al. 2014). Our results suggest that the opposite PK_k responses at lower and higher midlatitudes at high CO_2 values are linked to the contrasting responses in lower- and upper-tropospheric meridional temperature gradients and in lower and higher midlatitudes static stability. We note that while the changes in meridional temperature gradients are of the same sign across the midlatitudes, the position of the lower and higher midlatitude EKE within these gradients is different, which could result in different impacts of the baroclinicity of the storms.

We next analyze the evolution of the different Eady growth rate components as a function of CO_2 values (Fig. 6). Static stability in the higher (full green) and lower midlatitudes (dotted green) monotonically increases and decreases the baroclinicity, respectively, at most CO_2 levels. In the upper troposphere (black), $\partial\overline{T}/\partial y$ is positive and grows as CO_2 concentrations increase. Near the surface (gray), at low CO_2 values of 2× and 3×CO_2, the $\partial\overline{T}/\partial y$ response shows a very small weakening (Fig. 6a) or even strengthening (Fig. 6b), but at high CO_2 values, $\partial\overline{T}/\partial y$ robustly weakens. As a result, the increase in EKE at higher midlatitudes occurs at low and high CO_2 levels, while the decrease in EKE at lower midlatitudes occurs at higher CO_2 levels once after the near-surface $\partial\overline{T}/\partial y$ becomes more negative, and the static stability increases, and thus are strong enough to eliminate the scale-dependent response of the waves. The opposing responses of the lower- and upper-tropospheric meridional temperature gradient, with a strengthening aloft and reduction near the surface, and the increase and decrease in static stability at lower and higher midlatitudes, respectively, are evident in the zonal air temperature plots in both models (Fig. 7). The near-surface warming in the higher midlatitudes is less pronounced at 2×CO_2 (Figs. 7a,b) than at higher CO_2 values such as 4×CO_2 (Figs. 7c,d) and 8×CO_2 (Figs. 7e,f). Similar results are evident in the time evolution of the abrupt experiments, which further confirm the correlations found in Fig. 5. Specifically, the high-latitude EKE somewhat follows the fast evolution of the upper-tropospheric temperature changes, while the low-latitude EKE closely follows the slower lower-tropospheric changes (Fig. A2).

The reduced effect of the lower meridional temperature gradient at low CO_2 levels, in comparison to the large effect of the upper-level meridional temperature gradient, was also noted by Harvey et al. (2014) in the twenty-first-century projection scenarios. They demonstrated a strong correlation between the temperature gradients and storm tracks. In the higher midlatitudes, they found an EKE increase while the upper meridional temperature gradient strengthened. In the lower midlatitudes, Harvey et al. (2014) reported a minor increase in EKE coinciding with a minor strengthening of the meridional temperature gradient. These findings agree with the results of our study, which clarifies the "delayed" impact of the lower meridional temperature gradient at high CO_2 levels, particularly when polar amplification becomes prominent in the Southern Hemisphere.

Last, we wish to highlight that the air temperature response in the extended emissions scenarios (Fig. 8) closely mirrors the one in our idealized CO_2 experiments. By 2100 (Figs. 8c,d), we notice faster warming in the upper troposphere in the lower midlatitudes compared to the higher midlatitudes, inducing strengthening of the upper-tropospheric meridional temperature gradient that acts to strengthen the

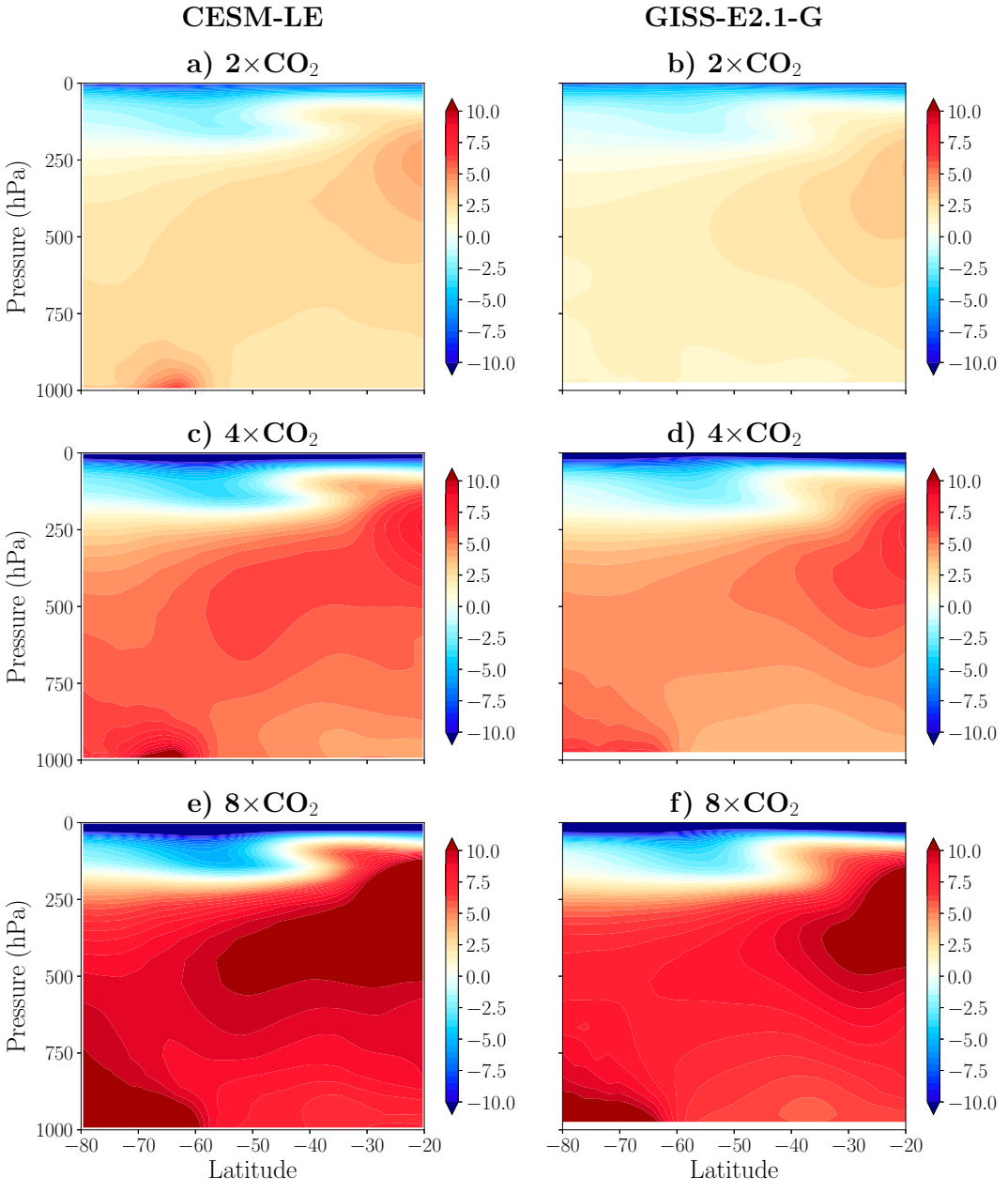

FIG. 7. SH winter (JJA) air temperature response in (a),(b) 2×CO_2; (c),(d) 4×CO_2; and (e),(f) 8×CO_2 for the last 50 years of the abrupt-CO_2 runs. The data from the (left) CESM-LE model and (right) GISS-E2.1-G model.

baroclinicity and EKE across all latitudes. The lower-tropospheric temperature gradient weakens, reducing EKE in lower midlatitudes, though the effect is minor compared to the weakening seen by 2200 (Figs. 8e,f) at a higher 7.4×CO_2 level. By 2300 (Figs. 8g,h), the lower-tropospheric gradient weakens even more, leading to a greater EKE reduction in lower midlatitudes. In addition, the static stability in all scenarios increases and decreases at lower and higher midlatitudes, respectively. This confirms that the temperature gradient mechanism in the idealized CO_2 experiments is also operative in the extended emission scenarios.

4. Discussion and conclusions

We have examined the behavior of Southern Hemisphere winter storm tracks through the analysis of eddy kinetic energy (EKE) during June–July–August (JJA) under high-CO_2 experiments using 1) the extended RCP8.5 and SSP5-8.5 scenarios and 2) experiments with two Earth system models with abrupt- and transient-CO_2 experiments. While previous studies using CMIP5 and CMIP6 models have generally reported an overall intensification of EKE in the Southern Hemisphere winter, our findings reveal a nonlinear response to increasing

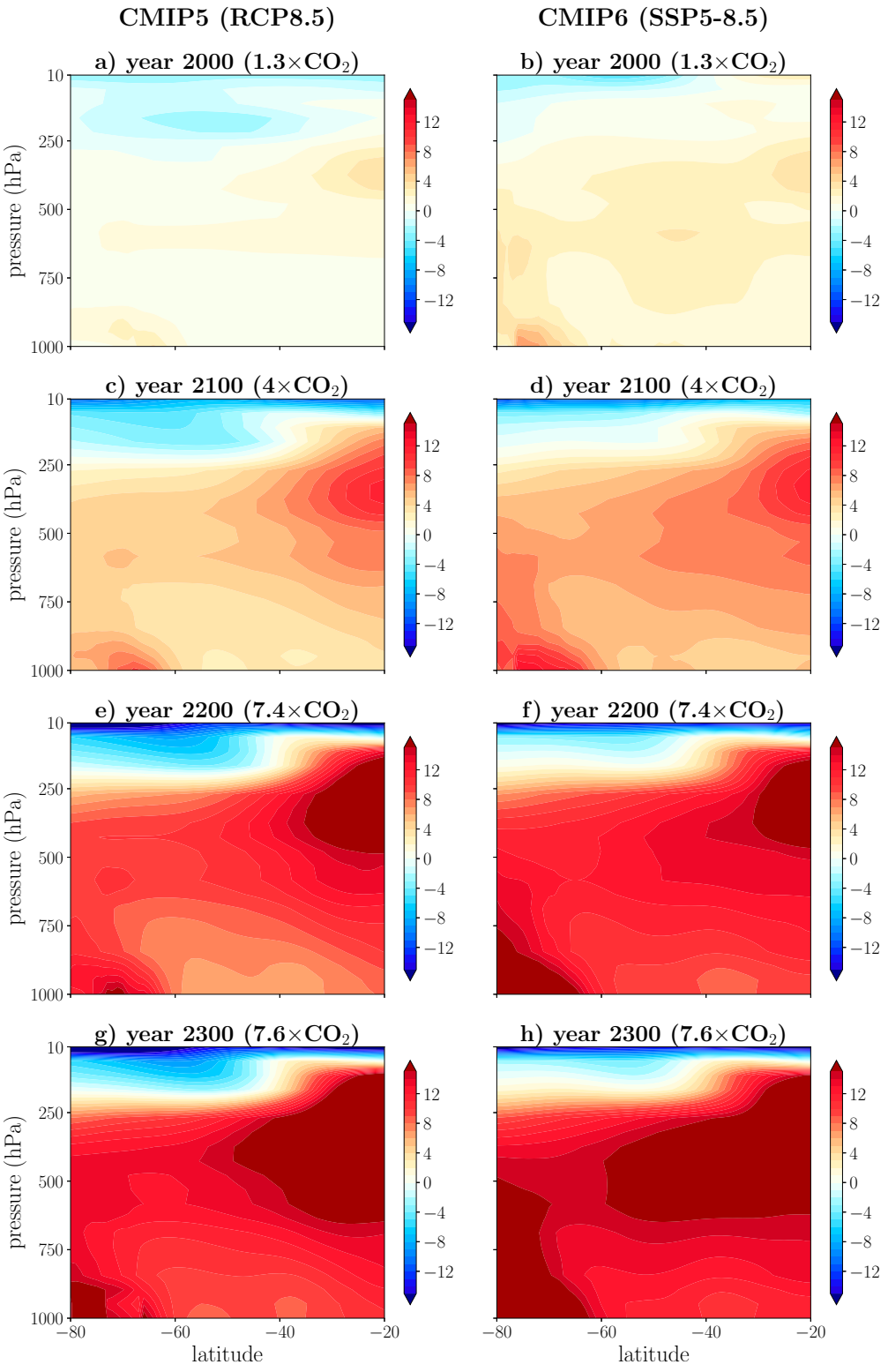

FIG. 8. Multimodel mean SH winter air temperature response in extended (left) RCP8.5 and (right) SSP5-8.5 scenarios up to (a),(b) year 2000; (c),(d) year 2100 with approximate 4×CO_2; (e),(f) year 2200 with 7.4×CO_2; and (g),(h) year 2300 with 7.6×CO_2.

CO_2 levels beyond 2100. Specifically, we find that at low CO_2 values, EKE strengthens at higher midlatitudes and to a lesser extent at lower midlatitudes. However, as CO_2 levels continue to rise, EKE weakens at lower midlatitudes and maintains its intensification at higher midlatitudes, thus shifting the EKE poleward.

We attribute the nonlinear EKE response to scale-dependent effects. At lower midlatitudes, long waves amplify while short waves attenuate, leading to only small EKE changes. At high CO_2 levels, the weakening of shorter waves outweighs the strengthening of longer waves, resulting in a decrease in EKE in the lower midlatitudes. By analyzing the spectral EKE budget, we have identified the conversion of eddy available potential energy to EKE (PK_k) as the primary driver of this scale-dependent response.

Further decomposition of the baroclinicity reveals that the nonlinear EKE response in the lower midlatitudes stems from the "tug of war" between the upper- and lower-tropospheric meridional temperature gradients, which have competing effects on the baroclinicity of the atmospheric flow, especially at large scales. A similar tug of war has been explored in the literature (O'Gorman 2010; Barnes and Polvani 2015; Vallis et al. 2015; Shaw et al. 2016) in the context of increasing CO_2 concentrations, but we here have shown its importance in explaining the nonlinear response at very high CO_2 values.

Last, the nonlinear response of EKE is somewhat different in the transient 1pctCO_2 simulations compared to the abrupt-CO_2 experiments. For example, in the 1pctCO2 runs, the EKE reduction in the lower midlatitudes is of a smaller magnitude compared to the one in the abrupt-CO_2 runs. This disparity can again be attributed to the tug of war between the response of the upper- and lower-tropospheric meridional temperature gradient. The lower-tropospheric temperature gradient is delayed in the 1pctCO_2 run because polar amplification takes longer to manifest itself in a transient run (compared to an abrupt run). A similar tug of war between the lower and upper temperature gradients can also be noted in the extended RCP8.5 and SSP5-8.5 runs between the years 2200 and 2300. There is little change in CO_2 from 7.4× to 7.6×CO_2, but the EKE reduction at year 2300 is almost one-third higher than at 2200.

In conclusion, our findings of a nonlinear response of the Southern Hemisphere winter storm tracks to high CO_2 concentrations have important implications for time-sensitive mitigation strategies in the highest emission scenario over the next century. Current approaches, focusing solely on increasing storminess, might need to be adapted. Mitigation strategies should account for the spatial heterogeneity of storm track activity, with some regions experiencing reduced storminess in a warmer world while the higher midlatitudes are expected to undergo increased storm track activity.

Acknowledgments. This work was supported by NASA FINESST Grant 80NSSC20K1657. The work of LMP is supported, in part, by a grant from the U.S. National Science Foundation to Columbia University. We thank the high-performance computing resources provided by NASA's Advanced Supercomputing (NAS) Division and the NASA Center for Climate Simulation (NCCS). Part of the computing and data storage resources, including the Cheyenne supercomputer (https://doi.org/10.5065/D6RX99HX), were provided by the Computational and Information Systems Laboratory at the National Center for Atmospheric Research (NCAR).

Data availability statement. The experiments with CESM-LE and GISS-E2.1-G models were previously analyzed in Mitevski et al. (2021, 2022, 2023). The CESM-LE model data can be obtained at https://doi.org/10.5281/zenodo.5725084 and GISS-E2.1-G model data at https://doi.org/10.5281/zenodo.3901624.

APPENDIX

Supplementary Figures

Figures A1–A11 are supplementary figures to the main text.

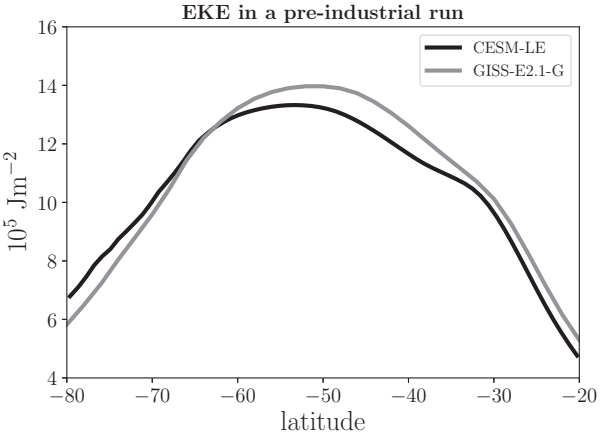

FIG. A1. Zonal wintertime EKE (10^6 J m^{-2}) in PI runs with CESM-LE (black) and GISS-E2.1-G (gray).

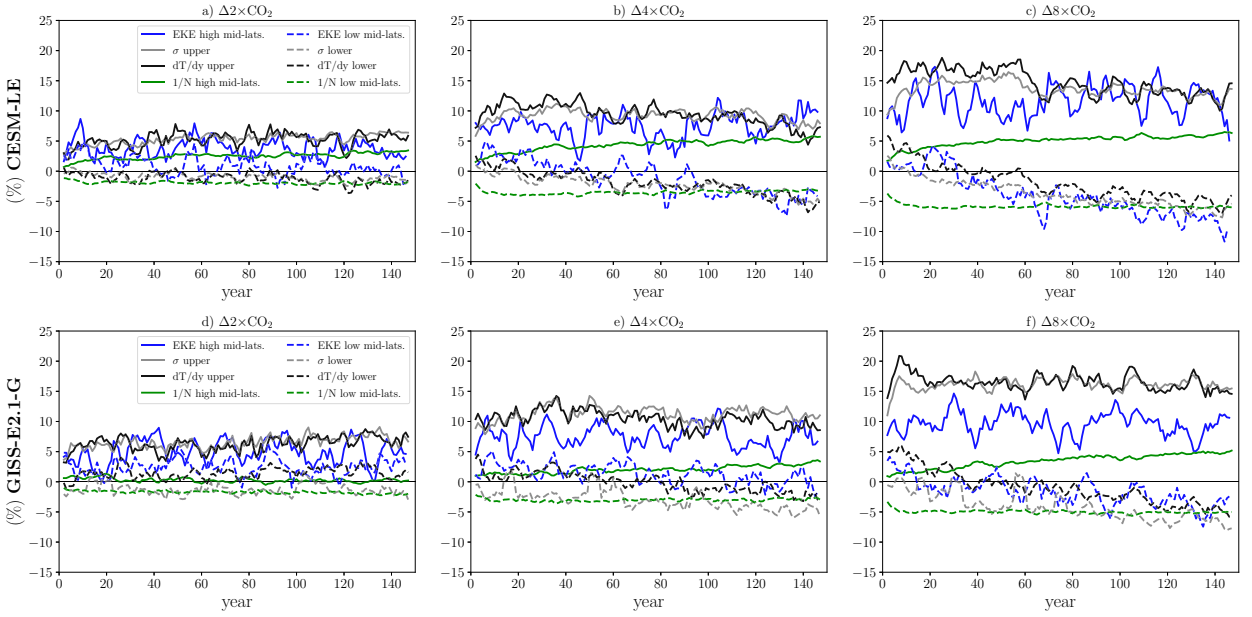

FIG. A2. Time series for the abrupt (a),(d) 2×CO_2; (b),(e) 4×CO_2; and (c),(f) 8×CO_2 for the (a)–(c) CESM-LE and (d)–(f) GISS. Vertically integrated EKE (blue) and inverse of static stability (green) at high (solid) and low (dashed) midlatitudes, and σ (gray) and temperature gradients (black) in the upper (solid) and lower (dashed) troposphere.

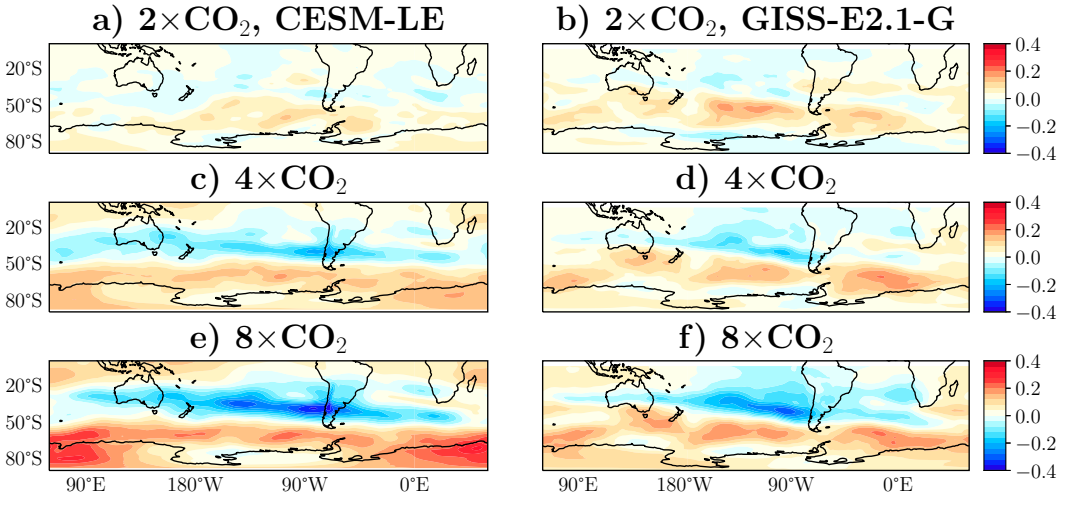

FIG. A3. Maps of wintertime EKE (10^6 J m^{-2}) response from PI for the abrupt (a),(b) 2×CO_2; (c),(d) 4×CO_2; and (e),(f) 8×CO_2 experiments. The data from the (left) CESM-LE model and (right) GISS-E2.1-G model.

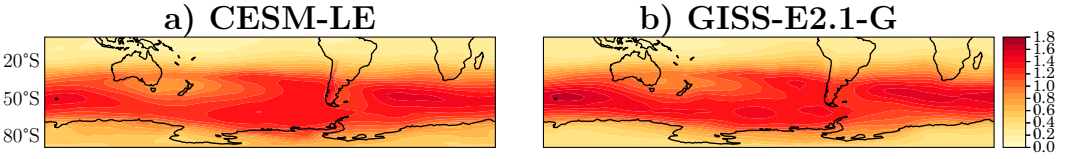

FIG. A4. Maps of wintertime EKE (10^6 J m^{-2}) for (a) CESM-LE and (b) GISS-E2.1-G models in the PI climatology.

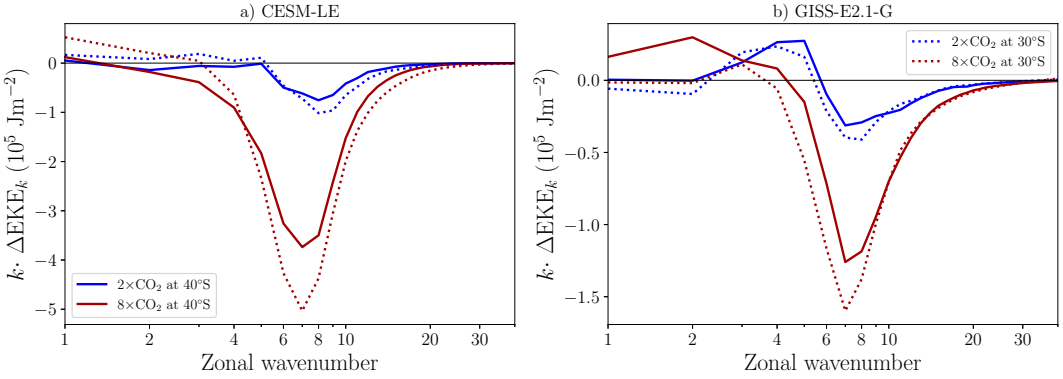

FIG. A5. The EKE_k response to increasing CO_2 levels (abrupt runs) as a function of zonal wavenumber in (a) CESM-LE and (b) GISS-E2.1-G models. The solid lines represent 40°S and dotted lines indicate 30°S. The EKE changes are multiplied by the zonal wavenumber to preserve the logarithmic x axis integral and are smoothed with a three-point running means for plotting purposes.

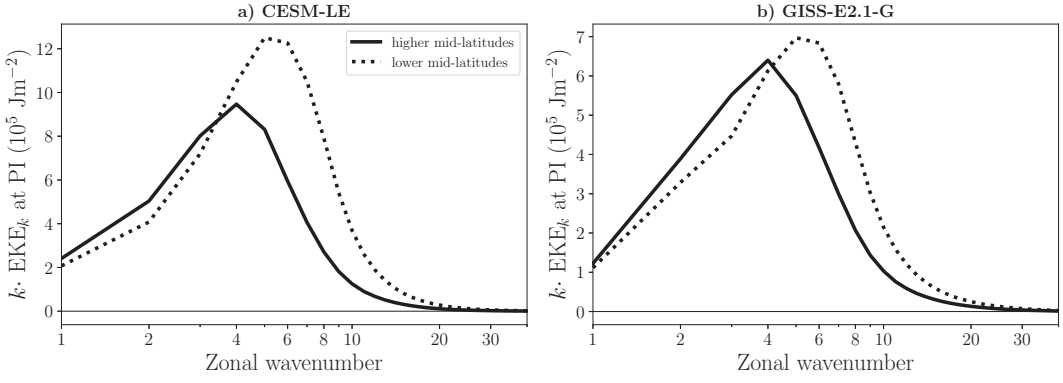

FIG. A6. As in Fig. 3, but for PI values.

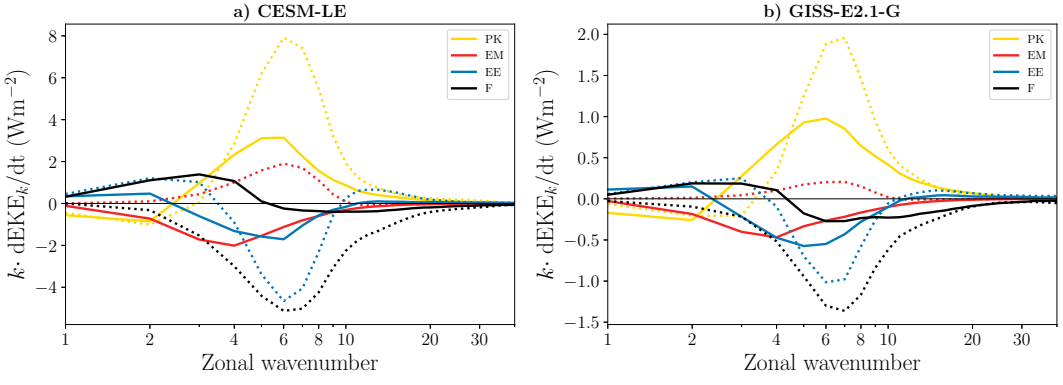

FIG. A7. As in Fig. 4, but for PI values.

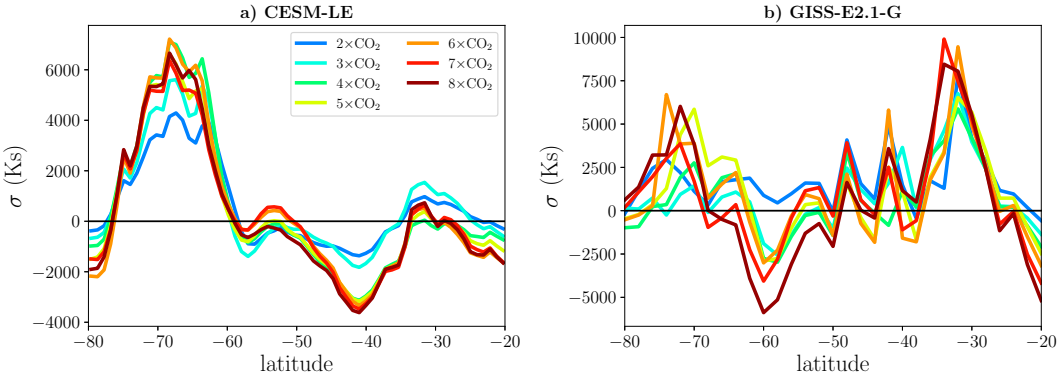

FIG. A8. Eady growth rate [$\sigma \propto (\partial \overline{T}/\partial y)/N$] integrated from 250 hPa to the surface for the (a) CESM-LE model and (b) the GISS-E2.1-G model shown for the range of 2× to 8×CO_2 for SH winter (JJA).

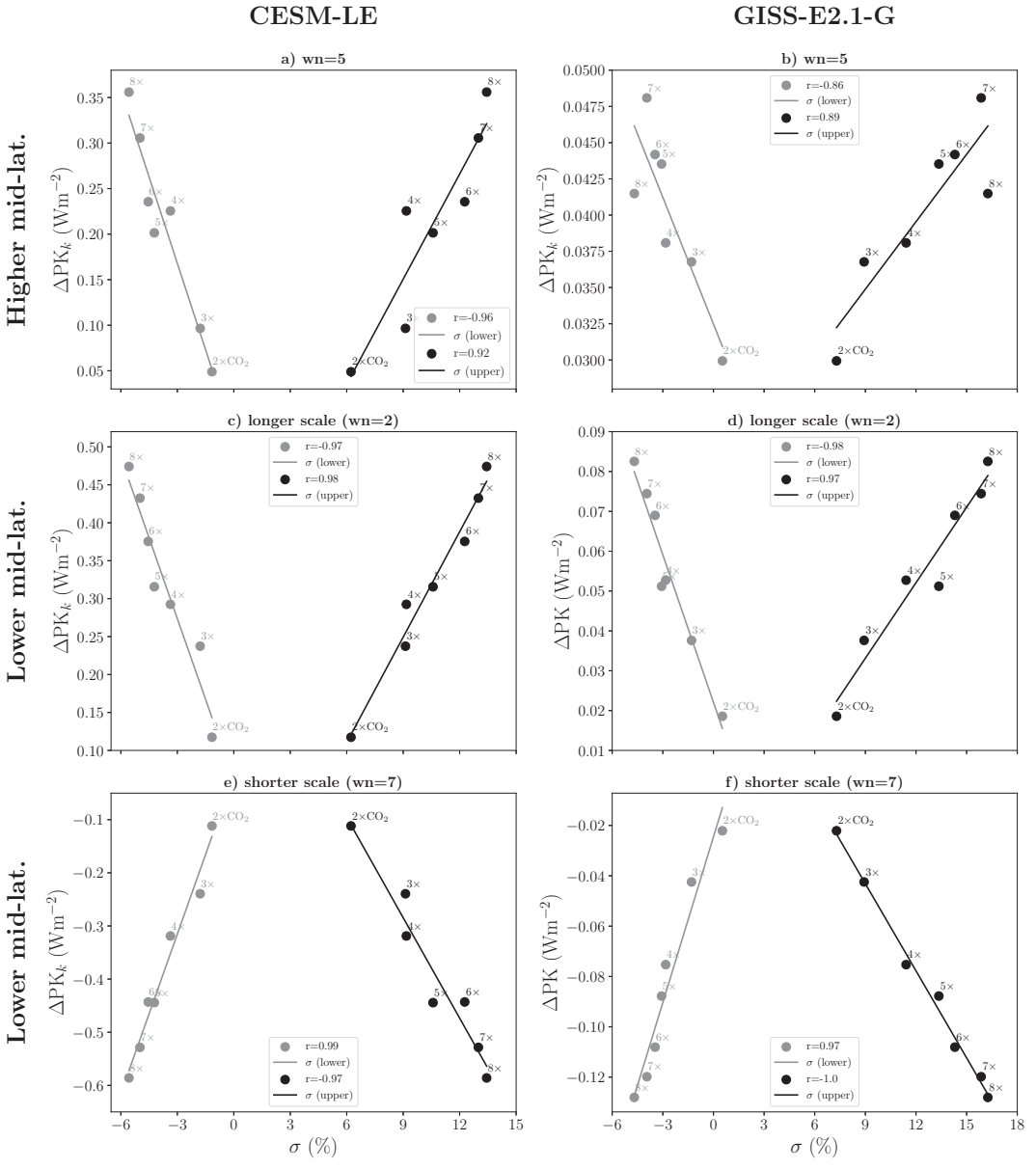

FIG. A9. Correlation between potential to kinetic energy conversion (PK_k) and upper (black) and lower (gray) tropospheric baroclinicity, as measured by the Eady growth rate $\sigma \propto [(\partial \overline{T}/\partial y)/N]$. The term $\partial \overline{T}/\partial y$ is the meridional temperature gradient, and N is the static stability. (a),(b) Higher midlatitudes, with longer waves (wavenumber 2) at lower midlatitudes shown in (c) and (d) and shorter waves (wavenumber 7) at lower midlatitudes in (e) and (f). The data from the (left) CESM-LE model and (right) GISS-E2.1-G model. The σ values are expressed as a percentage change from the $1\times CO_2$ values, while PK_k is presented as a difference from the $1\times CO_2$ values. The upper-tropospheric σ (black) is integrated from 250 to 500 hPa, while the lower-tropospheric σ from 500 hPa to the surface. The correlation coefficient (r value) is provided.

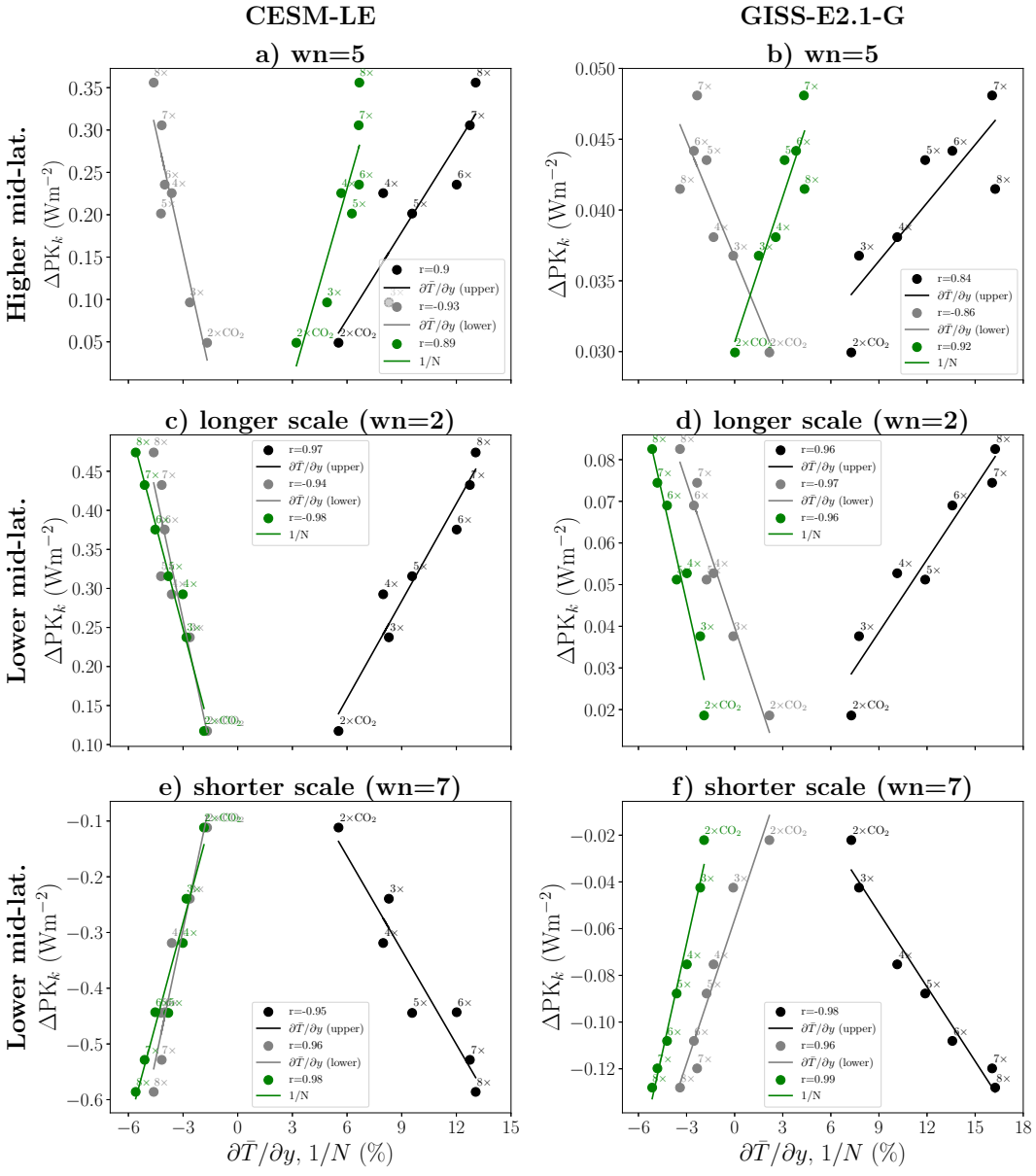

FIG. A10. Correlation between potential to kinetic energy conversion (PK_k) and upper (black) and lower (gray) meridional temperature gradient $\partial\overline{T}/\partial y$ and the inverse of static stability $1/N$. (a),(b) Higher midlatitudes, with longer waves (wavenumber 2) at lower midlatitudes shown in (c) and (d) and shorter waves (wavenumber 7) at lower midlatitudes in (e) and (f). The data from the (left) CESM-LE model and (right) GISS-E2.1-G model. The $\partial\overline{T}/\partial y$ and $1/N$ values are expressed as a percentage change from the $1\times CO_2$ values, while PK_k is presented as a difference from the $1\times CO_2$ values. The $1/N$ term is integrated from 250 hPa to the surface. The correlation coefficient (r value) is provided.

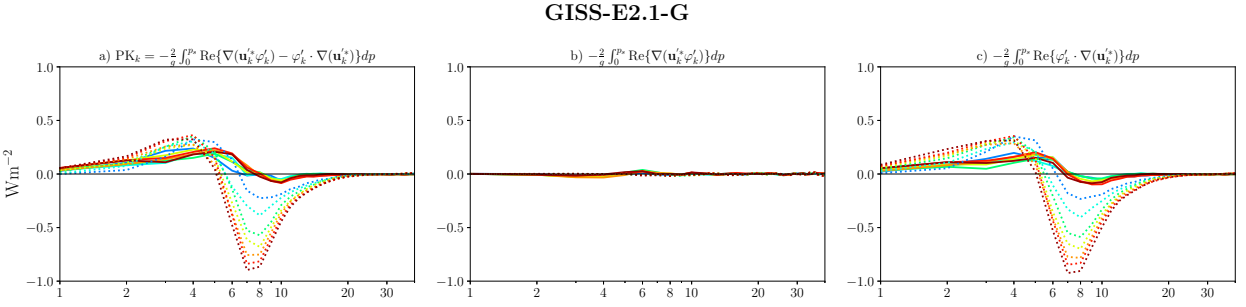

FIG. A11. Decomposition of the (a) PK_k equation [Eq. (4)] into the boundary term (b) $\nabla(\mathbf{u}_k'^* \varphi_k')$ and (c) $\mathbf{u}_k'^* \cdot \nabla(\varphi_k')$.

REFERENCES

Barnes, E. A., and L. M. Polvani, 2015: CMIP5 projections of Arctic amplification, of the North American/North Atlantic circulation, and of their relationship. *J. Climate*, **28**, 5254–5271, https://doi.org/10.1175/JCLI-D-14-00589.1.

Bender, F. A.-M., V. Ramanathan, and G. Tselioudis, 2012: Changes in extratropical storm track cloudiness 1983–2008: Observational support for a poleward shift. *Climate Dyn.*, **38**, 2037–2053, https://doi.org/10.1007/s00382-011-1065-6.

Butler, A. H., D. W. J. Thompson, and R. Heikes, 2010: The steady-state atmospheric circulation response to climate change–like thermal forcings in a simple general circulation model. *J. Climate*, **23**, 3474–3496, https://doi.org/10.1175/2010JCLI3228.1.

Chang, E. K. M., Y. Guo, and X. Xia, 2012: CMIP5 multimodel ensemble projection of storm track change under global warming. *J. Geophys. Res.*, **117**, D23118, https://doi.org/10.1029/2012JD018578.

Chang, E. K.-M., C.-G. Ma, C. Zheng, and A. M. Yau, 2016: Observed and projected decrease in northern hemisphere extratropical cyclone activity in summer and its impacts on maximum temperature. *Geophys. Res. Lett.*, **43**, 2200–2208, https://doi.org/10.1002/2016GL068172.

——, A. M.-W. Yau, and R. Zhang, 2022: Finding storm track activity metrics that are highly correlated with weather impacts. Part II: Estimating precipitation change associated with projected storm track change over Europe. *J. Climate*, **35**, 2423–2440, https://doi.org/10.1175/JCLI-D-21-0259.1.

Chemke, R., 2017: Atmospheric energy transfer response to global warming. *Quart. J. Roy. Meteor. Soc.*, **143**, 2296–2308, https://doi.org/10.1002/qj.3086.

——, and Y. Kaspi, 2015: The latitudinal dependence of atmospheric jet scales and macroturbulent energy cascades. *J. Atmos. Sci.*, **72**, 3891–3907, https://doi.org/10.1175/JAS-D-15-0007.1.

——, and Y. Ming, 2020: Large atmospheric waves will get stronger, while small waves will get weaker by the end of the 21st century. *Geophys. Res. Lett.*, **47**, e2020GL090441, https://doi.org/10.1029/2020GL090441.

——, ——, and J. Yuval, 2022a: The intensification of winter mid-latitude storm tracks in the Southern Hemisphere. *Nat. Climate Change*, **12**, 553–557, https://doi.org/10.1038/s41558-022-01368-8.

——, L. Zanna, C. Orbe, L. T. Sentman, and L. M. Polvani, 2022b: The future intensification of the North Atlantic winter storm track: The key role of dynamic ocean coupling. *J. Climate*, **35**, 2407–2421, https://doi.org/10.1175/JCLI-D-21-0407.1.

Coumou, D., J. Lehmann, and J. Beckmann, 2015: The weakening summer circulation in the northern Hemisphere mid-latitudes. *Science*, **348**, 324–327, https://doi.org/10.1126/science.1261768.

Fyfe, J. C., 2003: Extratropical Southern Hemisphere cyclones: Harbingers of climate change? *J. Climate*, **16**, 2802–2805, https://doi.org/10.1175/1520-0442(2003)016<2802:ESHCHO>2.0.CO;2.

Harvey, B. J., L. C. Shaffrey, and T. J. Woollings, 2014: Equator-to-pole temperature differences and the extra-tropical storm track responses of the CMIP5 climate models. *Climate Dyn.*, **43**, 1171–1182, https://doi.org/10.1007/s00382-013-1883-9.

——, P. Cook, L. C. Shaffrey, and R. Schiemann, 2020: The response of the Northern Hemisphere storm tracks and jet streams to climate change in the CMIP3, CMIP5, and CMIP6 climate models. *J. Geophys. Res. Atmos.*, **125**, e2020JD032701, https://doi.org/10.1029/2020JD032701.

Kay, J. E., and Coauthors, 2015: The Community Earth System Model (CESM) large ensemble project: A community resource for studying climate change in the presence of internal climate variability. *Bull. Amer. Meteor. Soc.*, **96**, 1333–1349, https://doi.org/10.1175/BAMS-D-13-00255.1.

Kelley, M., and Coauthors, 2020: GISS-E2.1: Configurations and climatology. *J. Adv. Model. Earth Syst.*, **12**, e2019MS002025, https://doi.org/10.1029/2019MS002025.

Lehmann, J., D. Coumou, K. Frieler, A. V. Eliseev, and A. Levermann, 2014: Future changes in extratropical storm tracks and baroclinicity under climate change. *Environ. Res. Lett.*, **9**, 084002, https://doi.org/10.1088/1748-9326/9/8/084002.

Lim, E.-P., and I. Simmonds, 2009: Effect of tropospheric temperature change on the zonal mean circulation and SH winter extratropical cyclones. *Climate Dyn.*, **33**, 19–32, https://doi.org/10.1007/s00382-008-0444-0.

Lorenz, E. N., 1955: Available potential energy and the maintenance of the general circulation. *Tellus*, **7A**, 157–167, https://doi.org/10.3402/tellusa.v7i2.8796.

Meinshausen, M., and Coauthors, 2020: The shared socio-economic pathway (SSP) greenhouse gas concentrations and their extensions to 2500. *Geosci. Model Dev.*, **13**, 3571–3605, https://doi.org/10.5194/gmd-13-3571-2020.

Mitevski, I., C. Orbe, R. Chemke, L. Nazarenko, and L. M. Polvani, 2021: Non-monotonic response of the climate system to abrupt CO_2 forcing. *Geophys. Res. Lett.*, **48**, e2020GL090861, https://doi.org/10.1029/2020GL090861.

——, L. M. Polvani, and C. Orbe, 2022: Asymmetric warming/cooling response to CO_2 increase/decrease mainly due to non-logarithmic forcing, not feedbacks. *Geophys. Res. Lett.*, **49**, e2021GL097133, https://doi.org/10.1029/2021GL097133.

——, Y. Dong, L. M. Polvani, M. Rugenstein, and C. Orbe, 2023: Non-monotonic feedback dependence under abrupt CO_2 forcing

due to a North Atlantic pattern effect. *Geophys. Res. Lett.*, **50**, e2023GL103617, https://doi.org/10.1029/2023GL103617.

O'Gorman, P. A., 2010: Understanding the varied response of the extratropical storm tracks to climate change. *Proc. Natl. Acad. Sci. USA*, **107**, 19 176–19 180, https://doi.org/10.1073/pnas.1011547107.

——, and T. Schneider, 2008: Energy of midlatitude transient eddies in idealized simulations of changed climates. *J. Climate*, **21**, 5797–5806, https://doi.org/10.1175/2008JCLI2099.1.

Orbe, C., and Coauthors, 2023: Atmospheric response to a collapse of the North Atlantic circulation under a mid-range future climate scenario: A regime shift in Northern Hemisphere dynamics. *J. Climate*, **36**, 6669–6693, https://doi.org/10.1175/JCLI-D-22-0841.1.

Peixóto, J. P., and A. H. Oort, 1974: The annual distribution of atmospheric energy on a planetary scale. *J. Geophys. Res.*, **79**, 2149–2159, https://doi.org/10.1029/JC079i015p02149.

Pfahl, S., and H. Wernli, 2012: Quantifying the relevance of cyclones for precipitation extremes. *J. Climate*, **25**, 6770–6780, https://doi.org/10.1175/JCLI-D-11-00705.1.

Polvani, L. M., D. W. Waugh, G. J. P. Correa, and S.-W. Son, 2011: Stratospheric ozone depletion: The main driver of twentieth-century atmospheric circulation changes in the Southern Hemisphere. *J. Climate*, **24**, 795–812, https://doi.org/10.1175/2010JCLI3772.1.

Priestley, M. D. K., and J. L. Catto, 2022: Future changes in the extratropical storm tracks and cyclone intensity, wind speed, and structure. *Wea. Climate Dyn.*, **3**, 337–360, https://doi.org/10.5194/wcd-3-337-2022.

Rivière, G., 2011: A dynamical interpretation of the poleward shift of the jet streams in global warming scenarios. *J. Atmos. Sci.*, **68**, 1253–1272, https://doi.org/10.1175/2011JAS3641.1.

Saltsman, B., 1957: Equations governing the energetics of the larger scales of atmospheric turbulence in the domain of wave number. *J. Meteor.*, **14**, 513–523, https://doi.org/10.1175/1520-0469(1957)014<0513:EGTEOT>2.0.CO;2.

Schwierz, C., P. Köllner-Heck, E. Zenklusen Mutter, D. N. Bresch, P.-L. Vidale, M. Wild, and C. Schär, 2010: Modelling European winter wind storm losses in current and future climate. *Climatic Change*, **101**, 485–514, https://doi.org/10.1007/s10584-009-9712-1.

Shaw, T. A., and Coauthors, 2016: Storm track processes and the opposing influences of climate change. *Nat. Geosci.*, **9**, 656–664, https://doi.org/10.1038/ngeo2783.

Tamarin-Brodsky, T., and Y. Kaspi, 2016: The poleward motion of extratropical cyclones from a potential vorticity tendency analysis. *J. Atmos. Sci.*, **73**, 1687–1707, https://doi.org/10.1175/JAS-D-15-0168.1.

——, and ——, 2017: Enhanced poleward propagation of storms under climate change. *Nat. Geosci.*, **10**, 908–913, https://doi.org/10.1038/s41561-017-0001-8.

Tamarin, T., and Y. Kaspi, 2017: Mechanisms controlling the downstream poleward deflection of midlatitude storm tracks. *J. Atmos. Sci.*, **74**, 553–572, https://doi.org/10.1175/JAS-D-16-0122.1.

Vallis, G. K., P. Zurita-Gotor, C. Cairns, and J. Kidston, 2015: Response of the large-scale structure of the atmosphere to global warming. *Quart. J. Roy. Meteor. Soc.*, **141**, 1479–1501, https://doi.org/10.1002/qj.2456.

Wu, Y., M. Ting, R. Seager, H.-P. Huang, and M. A. Cane, 2011: Changes in storm tracks and energy transports in a warmer climate simulated by the GFDL CM2.1 model. *Climate Dyn.*, **37**, 53–72, https://doi.org/10.1007/s00382-010-0776-4.

Yau, A. M.-W., and E. K.-M. Chang, 2020: Finding storm track activity metrics that are highly correlated with weather impacts. Part I: Frameworks for evaluation and accumulated track activity. *J. Climate*, **33**, 10 169–10 186, https://doi.org/10.1175/JCLI-D-20-0393.1.

Yin, J. H., 2005: A consistent poleward shift of the storm tracks in simulations of 21st century climate. *Geophys. Res. Lett.*, **32**, L18701, https://doi.org/10.1029/2005GL023684.

Yuval, J., and Y. Kaspi, 2020: Eddy activity response to global warming–like temperature changes. *J. Climate*, **33**, 1381–1404, https://doi.org/10.1175/JCLI-D-19-0190.1.

Zappa, G., L. C. Shaffrey, K. I. Hodges, P. G. Sansom, and D. B. Stephenson, 2013: A multimodel assessment of future projections of north Atlantic and European extratropical cyclones in the CMIP5 climate models. *J. Climate*, **26**, 5846–5862, https://doi.org/10.1175/JCLI-D-12-00573.1.